Polymer 51 (2010) 1056–1070

Contents lists available at ScienceDirect

Polymer

journal homepage: www.elsevier.com/locate/polymer

Morphology and properties of nanocomposites based on HDPE/HDPE-*g*-MA blends

M.W. Spencer, Lili Cui, Youngjae Yoo, D.R. Paul*

Department of Chemical Engineering and Texas Materials Institute, The University of Texas at Austin, Austin, TX 78712, United States

ARTICLE INFO

Article history:
Received 10 October 2009
Received in revised form
22 December 2009
Accepted 26 December 2009
Available online 18 January 2010

Keywords:
High density polyethylene (HDPE)
HDPE-*g*-MA
Nanocomposites

ABSTRACT

Nanocomposites formed from blends of high density polyethylene (HDPE) and maleic anhydride-grafted high density polyethylene (HDPE-*g*-MA) and $M_2(HT)_2$ organoclay were melt processed to explore the extent of exfoliation and the mechanical properties. Wide angle X-ray scattering (WAXS) and transmission electron microscopy (TEM) coupled with detailed particle analysis were used to determine the effect of HDPE-*g*-MA content and organoclay content on exfoliation and mechanical properties. As the HDPE-*g*-MA content increases, the global average particle aspect ratio initially increases drastically, reaches a maximum, and slightly decreases. The fraction of single platelets, however, increases at a steady rate for nanocomposites with HDPE-*g*-MA contents $\geq$25%. Relative modulus initially improves with increased levels of HDPE-*g*-MA, and then levels off with greater HDPE-*g*-MA content. Izod impact strength reaches a maximum at low HDPE-*g*-MA levels, decreases below the value for the pure HDPE nanocomposite, and levels off at higher HDPE-*g*-MA content. A composite model based on the Mori–Tanaka theory was developed to treat organoclay tactoids and single platelets as two separate types of fillers. This model gives rather good quantitative agreement between the predicted values of modulus calculated from the TEM results and that measured experimentally.

1. Introduction

Polymer nanocomposites based on organoclays can potentially lead to substantial enhancement in mechanical [1–3], barrier [4–6], thermal [7,8], and flammability [9–11] properties at very low filler concentrations while maintaining similar density and optical properties, making them attractive replacements for conventional composites. Melt mixing or compounding of polymer nanocomposites offers efficient exfoliation without the higher costs, complications, and environmental effects associated with in situ polymerization or solution blending. To obtain a well-exfoliated nanocomposite, with greatest property improvements, the individual organoclay platelets must interact favorably with the polymer matrix.

The structure of the ammonium surfactants used to modify montmorillonite (MMT) clay can be chosen to increase the affinity between the hydrophilic aluminosilicate clay and the organophilic polymer matrix. In our previous studies, nylon 6-based nanocomposites showed the best exfoliation with organoclays formed from a surfactant with only one long alkyl tail, allowing the polar polyamide more access to the silicate surface of the clay [1,12,13]. Non-polar polyolefin matrices, such as polypropylene or polyethylene, on the other hand, result in better exfoliation with organoclays modified by a surfactant with two or more long alkyl tails, providing increased alkyl–polyolefin interactions and decreased silicate–polyolefin interaction [3,14–16].

Nanocomposites formed from polyolefin matrices are often modified with a polar compatibilizer to improve exfoliation and enhance properties. The grafting of maleic anhydride to the polyolefin backbone significantly increases the polarity and, thus, improves exfoliation in polypropylene [3,17–24] and polyethylene [14,25–34]. Other approaches include the incorporation of polar comonomers like vinyl acetate [26,35,36], methacrylic acid [37–40], or methacrylic acid ionomers [16,41–43].

Maleated polypropylene, PP-*g*-MA, is typically used in relatively low quantities, comparable to the mass of organoclay, to form polypropylene-based nanocomposites and is thought of as a "compatibilizer" [19–24]. Use of small amounts of PP-*g*-MA is advantageous commercially owing to the substantially higher cost of PP-*g*-MA compared to unmodified PP. It would be useful, however, to understand how the morphology and properties of nanocomposites change as the ratio of maleated to unmaleated polyolefin in the matrix changes over a broader range.

* Corresponding author. Tel.: +1 512 471 5392; fax: +1 512 471 0542.
E-mail address: drp@che.utexas.edu (D.R. Paul).

0032-3861/$ – see front matter © 2010 Elsevier Ltd. All rights reserved.
doi:10.1016/j.polymer.2009.12.047

It is not practical to explore this question for polypropylene-based nanocomposites since the maleation process leads to significant scission of polypropylene chains, lowering the molecular weight and, therefore, greatly reducing the melt viscosity of PP-*g*-MA compared to the PP precursor [44–46]. Melt rheology is known to play some role in the exfoliation process in melt compounding since this affects the stresses imposed on the organoclay tactoids [13,47]. However, maleation of linear polyethylene does not lead to significant chain scission, making it possible to obtain commercial high density polyethylene (HDPE) and maleic anhydride-grafted high density polyethylene (HDPE-*g*-MA) with comparable rheological properties.

This paper explores the extent of organoclay exfoliation and the mechanical properties of melt compounded nanocomposites with matrices consisting of HDPE/HDPE-*g*-MA blends over the full range of compositions. This allows a useful way to explore the relationship between mechanical properties and the degree of exfoliation without dramatically changing the nature of the polymer matrix and to obtain further insights into the "compatibilizing" role of maleated polyolefins for nanocomposite formation.

2. Experimental

2.1. Materials

Table 1 summarizes the materials used in this study. The high density polyethylene, HDPE, (Alathon® M6020, LyondellBasell) and the maleic anhydride-grafted high density polyethylene, HDPE-*g*-MA, (Fusabond® E MB100D, Du Pont) were chosen because they have the same melt index (MI = 2 g/10 min). It is expected that the HPDE and the HDPE-*g*-MA used are miscible with each other based on prior work with related polyolefins [48,49]. The organoclay designated as $M_2(HT)_2$, donated by Southern Clay Products, was prepared by a cation exchange reaction between sodium montmorillonite (Na^+ MMT) and a two-tailed quaternary ammonium surfactant, dimethyl bis(hydrogenated-tallow) ammonium chloride (Arquad 2HT-75). Some frequently used abbreviations are employed here to represent the substituents on the ammonium cation, e.g., M for methyl and HT represents long alkyl chains from hydrogenated-tallow [1,16,50]. This organoclay was selected based upon recent studies showing improved organoclay exfoliation in polyethylene using surfactants with two tails on the ammonium ion instead of one tail [14,16,35,38]. The polymers employed have better affinity for the largely aliphatic organic modifier than for the unmodified clay surface. The larger area of the clay surface covered by two tails increases the favorable surfactant–polymer interaction and decreases the unfavorable polymer–clay interaction.

2.2. Melt processing

The organoclay and the HDPE-*g*-MA were dried for a minimum of 24 h in a vacuum oven at 80 °C, prior to melt processing. Nanocomposites were melt compounded in a Haake co-rotating, intermeshing twin screw extruder (diameter = 30 mm, $L/D = 10$) using a barrel temperature of 200–205 °C, a screw speed of 280 rpm, and a feed rate of 1 kg/h. The HDPE, the HDPE-*g*-MA, and the organoclay were hand-mixed prior to extrusion and introduced into the extruder by a single hopper.

Tensile specimens (ASTM D638, Type I) and Izod bars (ASTM D256) were prepared by an Arburg Allrounder 305-210-700 injection-molding machine using a barrel temperature of 200 °C (feed) to 205 °C (die), an injection pressure of 75 bar, and a holding pressure of 50 bar. After molding, the samples were immediately sealed in a polyethylene bag and placed in a vacuum desiccator for a minimum of 24 h prior to testing.

The montmorillonite content of the nanocomposite was determined by placing pre-dried nanocomposite pellets in a furnace at 900 °C for 45 min and weighing the remaining MMT ash, correcting for loss of structural water [13,51–53].

2.3. Characterization

Differential scanning calorimetric (DSC) thermograms were recorded using a Perkin–Elmer Model DSC-7 at a heating rate of 10 °C/min under an extra dry N_2 atmosphere over a temperature range of 30–180 °C. The pre-dried neat HDPE and HDPE-*g*-MA samples of 7–10 mg were packed in aluminum pans, heated to 180 °C, and held there for 5 min to reset the thermal history. The melting temperature and the heat of fusion were determined from the second heating scan. The percent crystallinity was determined by dividing the heat of fusion value by 293 J/g, the heat of fusion of 100% crystalline polyethylene [54].

Morphology was examined primarily via a JEOL 2010F transmission electron microscope (TEM) operating under an accelerating voltage of 120 kV. Some samples were observed using a FEI TECNAI G2 F20 X-TWIN TEM operating under an accelerating voltage of 200 kV. Ultra-thin sections (~50 nm) for morphological analysis were taken from the core portion of an injection-molded bar in the plane defined by the flow direction (FD) and the normal direction (ND) using an RMC PowerTome XL microtome [55]. The nanocomposite samples and the diamond knife were cooled to between −75 and −85 °C and −60 °C, respectively, using liquid nitrogen. Cut sections were collected onto 400 mesh grids and dried with filter paper.

Wide angle X-ray scattering (WAXS) scans were performed using a Bruker-AXS D8 Advance diffractometer in the reflection

Table 1
Materials used in this study.

Material	Commercial designation	Specifications	Supplier
Polymer			
HDPE	Alathon® M6020	MI = 2 g/10 min Density = 0.96 g/cm^3	LyondellBasell
HDPE-*g*-MA	Fusabond® E MB100D	MI = 2 g/10 min Density = 0.96 g/cm^3 Melting point = 134 °C MA content = 0.9 wt%	Du Pont
Organoclay			
$M_2(HT)_2$	*Cloisite® 20A*: Dimethyl bis(hydrogenated-tallow) ammonium montmorillonite	Organic loading = 95 mequiv/100 g clay Organic content = 39.6 wt% d_{001} spacing = 24.2 Å Density = 2.83 g/cm^3	Southern Clay Products

mode, using an incident X-ray wavelength of 0.1541 nm at a scan rate of 3.0°/min over the range of $2\theta = 1°–12°$. The skin of the major face of the rectangular nanocomposite bars and the organoclay powder were scanned [56].

Tensile tests were performed according to ASTM D638 using an Instron model 1137 machine upgraded for computerized data acquisition. Tensile modulus values were determined using an extensometer at a crosshead rate of 0.51 cm/min and averaged from at least five specimens. Elongation at break and yield strength data were taken at 0.51 cm/min and averaged from at least three specimens. Elongations greater than 400% could not be measured, due to the limitations of crosshead travel.

Notched Izod impact tests were conducted at room temperature using a 6.8 J hammer and 3.5 m/s impact velocity using a TMI Impact tester (model 43-02). Standard notches were made according to ASTM D256. Frequently, as-molded rectangular bars are cut in half (to generate more samples) and the Izod impact strength data from the gate end (the end at which the molten polymer enters the mold during injection molding) and the far end are averaged together. Morphological differences arising from the injection-molding process can result in significant differences between the Izod impact strength measured at the gate end and the far end of the samples. Thus, in this work, the Izod impact strength data were averaged from four samples each of the gate end, of the middle, and of the far end of the bars.

2.4. Particle analysis

Particle analyses were performed on TEM micrographs at magnifications of 8–30 K, depending on the extent of exfoliation in the sample. Because of low contrast, TEM images were converted into .jpg format and opened in GIMP (GNU Image Manipulation Program). Two tracings in separate, transparent layers were made of particle length and thickness. For nanocomposites with single platelets, the thickness of these platelets could not accurately be measured and was assigned a thickness of 0.94 nm corresponding to the known results for MMT platelets [35,57]. Each tracing was saved separately in .tif format and imported into the image analysis program, SigmaScan Pro, where each particle tracing was assigned a number and their characteristic dimensions were measured. Since the numbers assigned in the tracing of the length and the tracing of the thickness of the particles do not correspond, the particle dimensions must be matched manually. In this work, four different kinds of aspect ratios are calculated, i.e., the number and weight averages of the aspect ratios calculated for individual particles, $\langle l/t\rangle_n$ and $\langle l/t\rangle_w$, and ratios of the number and weight averages of particle lengths and thicknesses, $(\overline{l_n}/\overline{t_n})$ and $(\overline{l_w}/\overline{t_w})$. To ensure statistical validity of the analysis, 200–400 particles were counted to measure the length, thickness, and aspect ratio. The results are summarized in Table 2.

3. Results and discussion

3.1. Properties of neat blends

Before discussing the morphology and properties of the nanocomposites, it is useful to examine the properties of the neat HDPE/HDPE-*g*-MA blends used as nanocomposite matrices. The melting temperature (peak values), heat of fusion, and percent crystallinity for neat HDPE and HDPE-*g*-MA are shown in Table 3, as determined by DSC. HDPE-*g*-MA has lower melting temperature, heat of fusion and degree of crystallinity than HDPE, due to the maleic anhydride groups that disrupt the ordered crystalline structure of polyethylene.

The tensile modulus and the yield strength of neat HDPE/HDPE-*g*-MA blends are shown plotted versus HDPE-*g*-MA content in Fig. 1(a) and (b) respectively. Both modulus and yield strength decrease at high HDPE-*g*-MA levels, likely due to the lower crystallinity of HDPE-*g*-MA compared with HDPE. Neat blends of HDPE/HDPE-*g*-MA are too ductile to determine the breaking point on the available equipment, therefore, all elongations at break are >400%.

Neat HDPE has been reported to have different impact values for the gate end and far end of injection-molded Izod bars [58]. Because of large differences measured between the ends in this work, impact strengths were averaged separately for the gate and far ends. In addition, impact strengths were measured at the middle of the Izod bars by cutting off the quarters of the bar near the gate and far end. Izod impact strength data for neat HDPE/HDPE-*g*-MA blends are presented in Fig. 1(c). Generally, the fracture energy decreases from the gate end to the middle and from the middle to the far end. This could be the result of differences in the molecular orientation, crystal orientation, and percent crystallinity along the length of the bar. Pantani et al. found significant changes in molecular orientation along the flow direction, but no significant change in crystallinity, for injection-molded isotactic polypropylene (iPP). They also noted substantial morphological differences by varying the molding conditions [59,60]. In our study, the molding conditions were held relatively constant. The molding conditions may be optimized to minimize the difference in impact strength along the flow direction of the bar, but this was beyond the scope of this work.

Izod impact strength generally decreases as HDPE-*g*-MA content increases regardless of the portion of the bar tested. At ~6% HDPE-*g*-MA the fracture energy decreases dramatically. Higher levels of HDPE-*g*-MA reduce the impact strength more gradually. Bars with HDPE-*g*-MA levels of <5% have a large variance in impact strength.

Table 2
Results of one population particle analysis of nanocomposites.

HDPE-*g*-MA (%)	Wt% MMT	Mass HDPE-*g*-MA/Mass organoclay	Total number of particles	Number average particle length ($\overline{l_n}$, nm)	Number average particle thickness ($\overline{t_n}$, nm)	Weight average particle length ($\overline{l_w}$, nm)	Weight average particle thickness ($\overline{t_w}$, nm)	Number average aspect ratio ($\overline{l_n}/\overline{t_n}$)	Number average aspect ratio $\langle l/t\rangle_n$	Weight average aspect ratio ($\overline{l_w}/\overline{t_w}$)	Weight average aspect ratio $\langle l/t\rangle_w$
0	5.05	0	206	315.6	23.7	568.1	56.4	13.3	20.3	10.1	30.7
0.5	5.29	0.05	225	289.5	15.1	430.4	33.1	19.2	29.0	13.0	40.5
3	4.87	0.34	221	213.1	9.6	271.1	18.7	22.2	33.1	14.5	46.3
9	4.94	1.01	321	196.2	4.6	256.7	8.5	42.8	58.4	30.2	82.2
18	5.13	1.94	336	99.4	2.3	128	7.0	43.7	55.7	18.3	67.5
25	5.2	2.65	340	97.5	1.7	126.5	2.2	57.6	62.1	58.4	76.1
50	5.41	5.08	408	84.9	1.4	109.4	3.3	59.8	64.9	33.6	76.0
65	5.3	6.76	349	73.5	1.2	90.8	1.6	59.2	60.5	55.2	70.2
85	5.31	8.81	355	66.2	1.2	79.9	1.2	56.8	57.8	65.1	68.8
100	5.37	10.25	362	55.5	1.1	70.2	1.2	48.7	48.2	59.1	57.4

Table 3
DSC results for neat polymers.

Material	T_m (°C)	ΔH_m (J/g)	% Crystallinity
HDPE	136.7	193.2	65.9
HDPE-*g*-MA	133.5	175.0	59.7

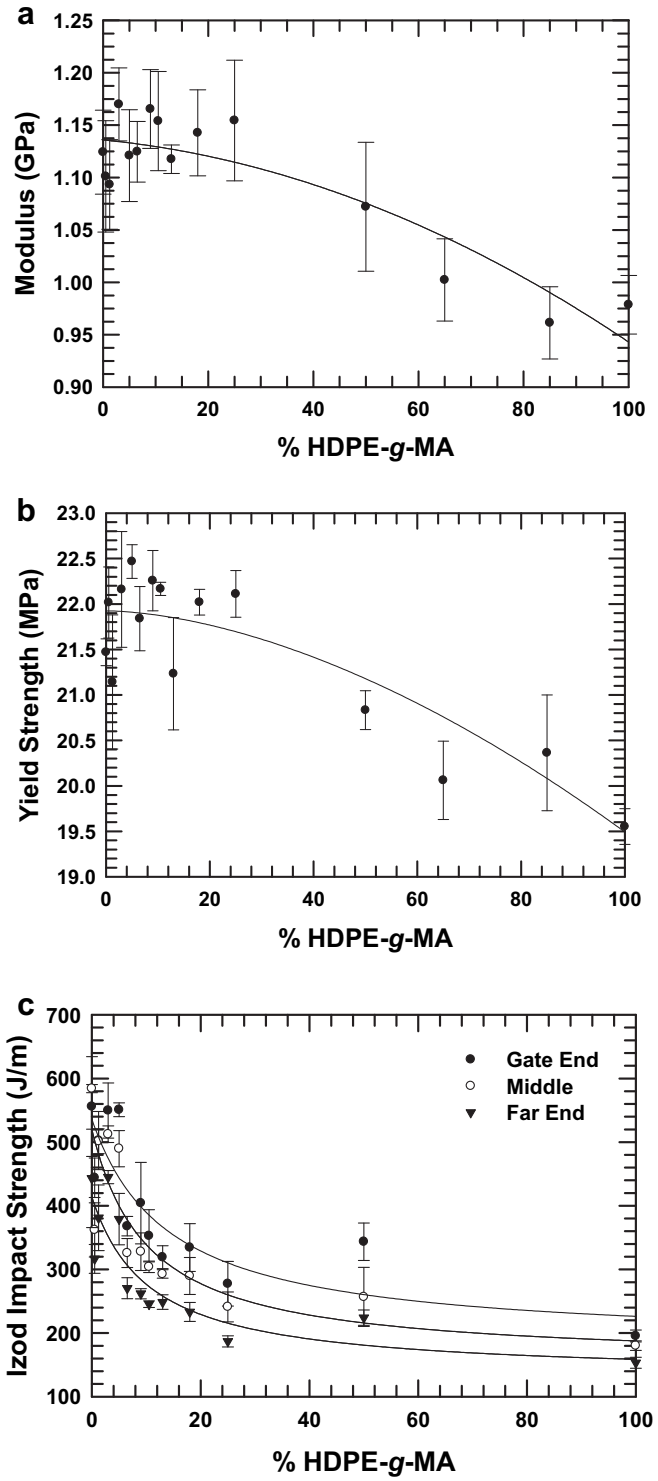

Fig. 1. Effect of HDPE-*g*-MA content on mechanical properties of HDPE/HDPE-*g*-MA blends without clay: (a) tensile modulus, (b) yield strength, and (c) Izod impact strength.

The change in impact strength with increased HDPE-*g*-MA content was not expected and the reasons are not well understood. Molding conditions such as injection speed were varied for both neat HDPE and neat HDPE-*g*-MA, but the Izod impact strength for HDPE was always significantly higher than for HDPE-*g*-MA. Differences in crystallinity, interactions between maleic anhydride groups, and differences in the molecular weight distributions may affect the fracture energy; however, sorting out these and possibly other reasons for the differences shown was considered to be beyond the scope of this paper.

3.2. Morphology

3.2.1. Transmission electron microscopy

TEM observations allow for a visual, qualitative assessment of the degree of organoclay exfoliation in polymer nanocomposites. Fig. 2 shows representative TEM micrographs for nanocomposites with different HDPE-*g*-MA concentrations having a nominal MMT content of 5 wt%. For the HDPE nanocomposites (Fig. 2(a)), large tactoids are seen, indicating poor clay dispersion. Particles with thicknesses of 1 μm or greater can be found.

The addition of merely 0.5 wt% HDPE-*g*-MA (Fig. 2(b)) to the polymer matrix significantly improves the exfoliation of the organoclay. Taking note of the different scale bars, the size of tactoids is decreased dramatically. Though large tactoids are still present, many smaller particles are seen. Clearly, even small amounts of HDPE-*g*-MA dramatically influence the ability of the polymer matrix to exfoliate the organoclay.

As more HDPE-*g*-MA is added to the polymer matrix, exfoliation continues to improve. As seen in Fig. 2(c), (d), and (e), for nanocomposites with 3 wt%, 9 wt%, and 18 wt% of HDPE-*g*-MA respectively, the size of the clay tactoids continue to decrease and the ratio of smaller particles to larger tactoids increases with increased polar content.

Nanocomposites based on 25 wt%, 50 wt%, 65 wt%, 85 wt%, and 100 wt% HDPE-*g*-MA are shown in Fig. 2(f), (g), (h), (i), and (j), respectively, and have a well-exfoliated morphology consisting primarily of single platelets. Little difference in the extent of exfoliation can be seen qualitatively.

The noted enhancements in exfoliation with increased amounts of polar MA groups in the polymer matrix indicate improved interactions between the polymer and the organoclay. The exfoliation improves rapidly with the addition of initial amounts of HDPE-*g*-MA, but after a certain threshold value is reached (~25 wt% HDPE-*g*-MA), little change in the extent of exfoliation is seen.

3.2.2. Particle analysis

Particle analysis is used to quantify the extent of exfoliation shown in the TEM images. The statistical results and the MMT concentration of each nanocomposite as determined by incineration are shown in Table 2. The aspect ratios obtained by averaging the values of each particle, $\langle l/t\rangle_n$ and $\langle l/t\rangle_w$, are generally larger than those calculated from the ratio of the corresponding average values of length and thickness, $(\overline{l_n}/\overline{t_n})$ and $(\overline{l_w}/\overline{t_w})$. The ratio of number average particle length and thickness, $(\overline{l_n}/\overline{t_n})$, is generally larger than the ratio of weight average particle length and thickness, $(\overline{l_w}/\overline{t_w})$ while the weight average aspect ratio obtained by averaging values of each particle, $\langle l/t\rangle_w$, is always larger than the corresponding number average ratio, $\langle l/t\rangle_n$. These trends are in a good agreement with previous reports [15,35,61].

Fig. 3 shows a series of representative histograms of particle length, thickness and aspect ratio for HDPE/HDPE-*g*-MA 25% based nanocomposites containing ~5 wt% MMT. All of these features showed broad distributions based on the analysis of a total of 340

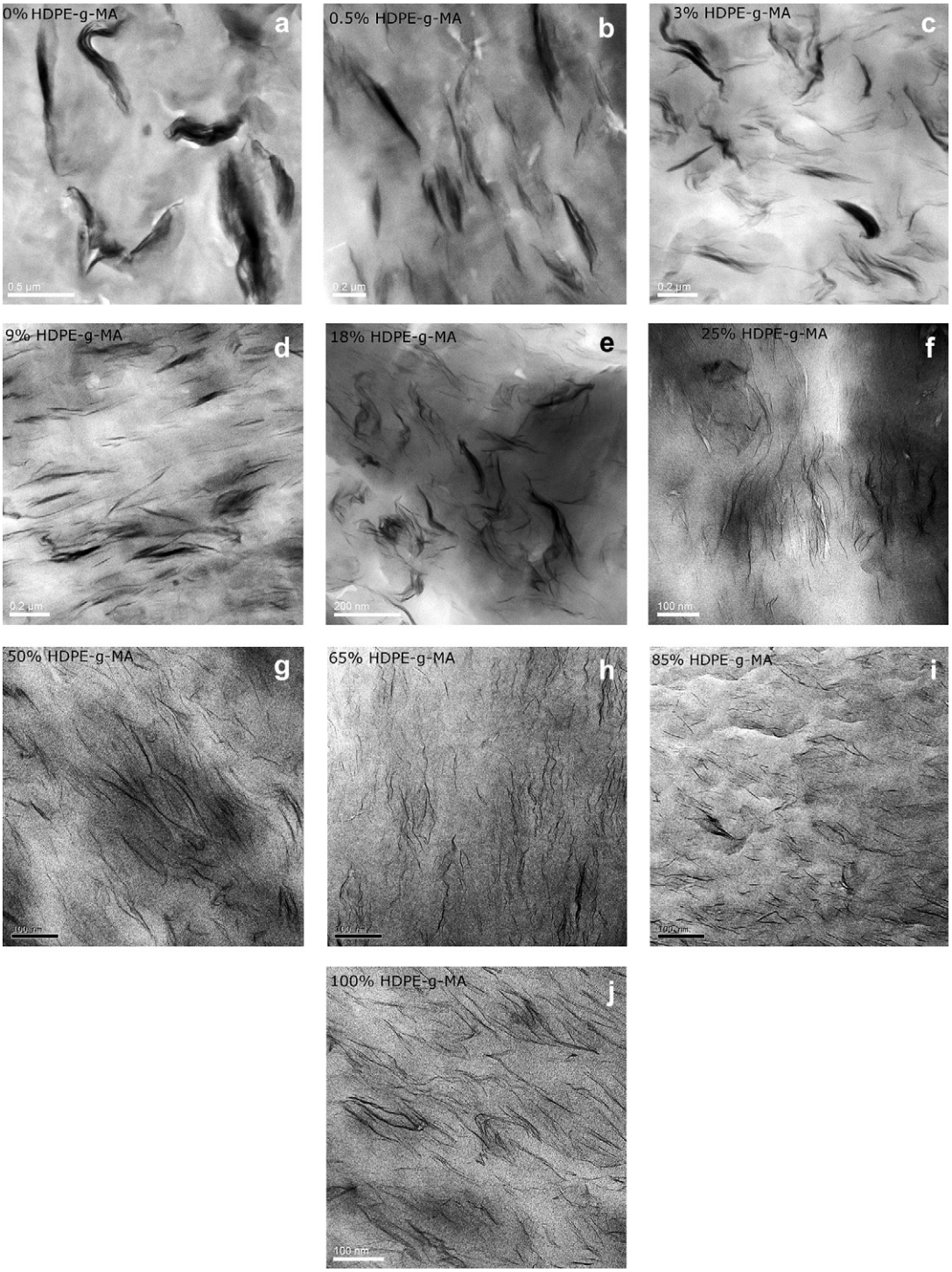

Fig. 2. TEM photomicrographs of HDPE/HDPE-*g*-MA/ $M_2(HT)_2$ nanocomposites with nominally 5 wt% MMT: (a) HDPE, (b) HDPE/HDPE-*g*-MA 0.5%, (c) HDPE/HDPE-*g*-MA 3%, (d) HDPE/HDPE-*g*-MA 9%, (e) HDPE/HDPE-*g*-MA 18%, (f) HDPE/HDPE-*g*-MA 25%, (g) HDPE/HDPE-*g*-MA 50%, (h) HDPE/HDPE-*g*-MA 65%, (i) HDPE/HDPE-*g*-MA 85%, and (j) HDPE-*g*-MA 100%.

particles. To better understand the relationship between the polarity of the polymer matrix and the organoclay exfoliation, plots of particle lengths and thicknesses (Fig. 4(a) and (b)) and particle aspect ratios (Fig. 4(c)) as a function of HDPE-*g*-MA content in the polymer matrix are presented for nanocomposites containing ~5 wt% MMT.

The quantitative trends mirror the qualitative TEM results discussed above. Average particle thickness and length decrease rapidly upon the addition of even small amounts of HDPE-*g*-MA. When the particle thickness decreases at a higher rate than the particle length, the aspect ratio increases. At HDPE-*g*-MA contents of 9% and 18% the length and thickness continue to decrease, but not as rapidly, indicating smaller improvements in exfoliation. For nanocomposites based on blends with HDPE-*g*-MA contents of ≥25%, the average particle thickness deceases gradually, due to the particle thickness limit of a single platelet (0.94 nm). Because the average particle length decreases at a greater rate than the particle thickness, the aspect ratio gradually decreases for matrices at >50% HDPE-*g*-MA content.

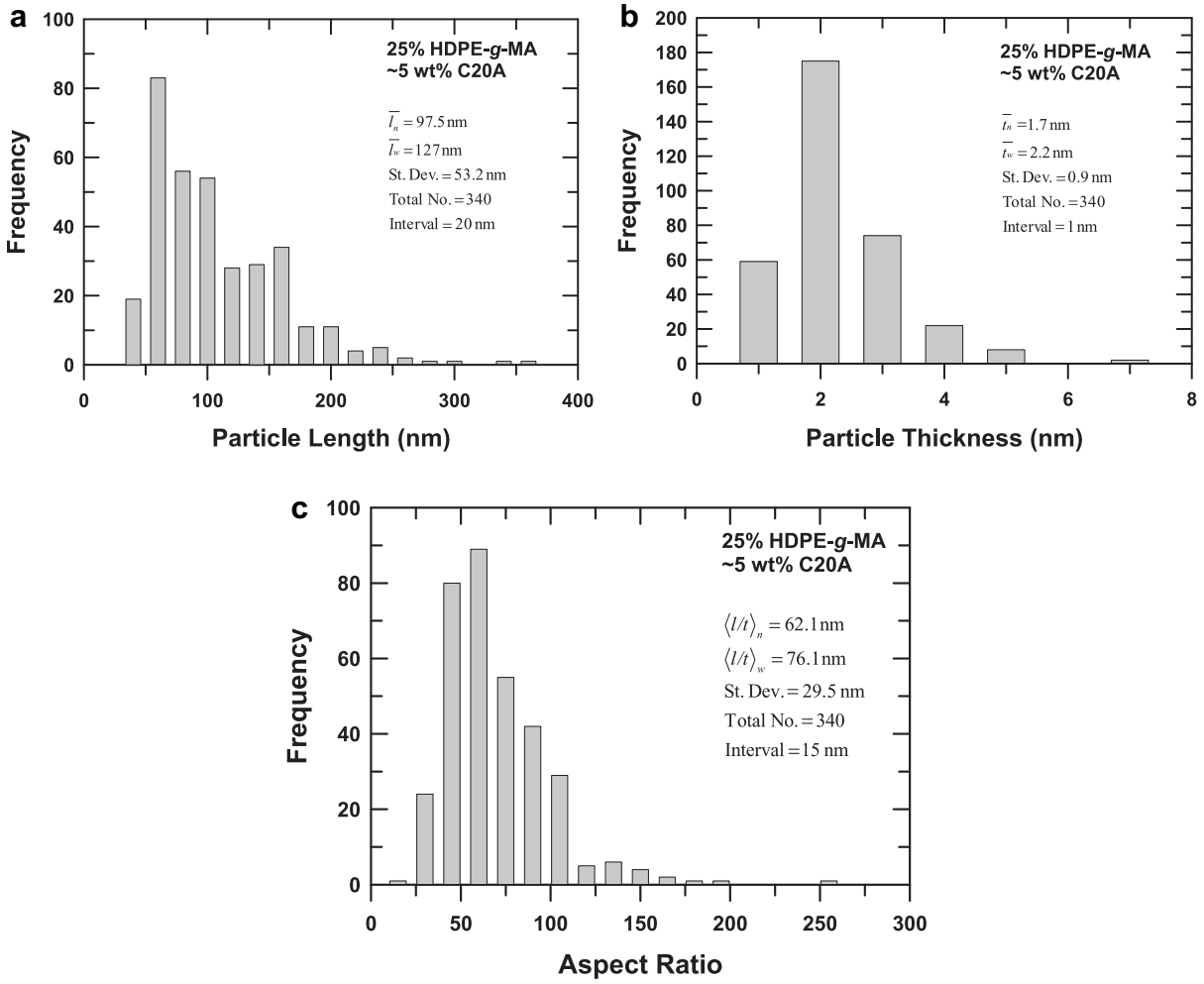

Fig. 3. Histograms of (a) particle length, (b) particle thickness, and (c) aspect ratio of HDPE/HDPE-*g*-MA 25%/$M_2(HT)_2$ nanocomposites for one population with nominally 5 wt% MMT (total number of particles = 340).

For further insight, the fraction of single platelets (Fig. 4(d)) was calculated by dividing the number of particles with a thickness of nearly 1 nm by the total number of particles. The fraction of single platelets increases with increasing HDPE-*g*-MA content for nanocomposites with >20% HDPE-*g*-MA. As the amount of single platelets increases, the average particle thickness decreases at a slower rate due to the thickness limit of a single platelet. Increased particle breakup and lower numbers of overlapping particles, however, continues to decrease the average particle length, resulting in a decreased aspect ratio.

Since partially exfoliated organoclay tactoids and fully exfoliated single platelets have differing reinforcement effects on the nanocomposites, these two populations of particles were also analyzed separately. The number average aspect ratio, $\langle l/t \rangle_n$, is shown for both single platelets with measured thicknesses of about 1 nm and for the remaining tactoids in Fig. 5 and Table 4. Surprisingly there is not a significant difference in the trends of these two populations. The decrease in single platelet aspect ratio may be attributed to lower amounts of slightly overlapping particles that are measured as single platelets and to increased particle breakup.

A schematic illustration of the change in particle dimensions for increased levels of HDPE-*g*-MA is shown in Fig. 6. Initially, particle thickness decreases faster than particle length, increasing the aspect ratio. As the average particle thickness approaches the limit of the platelet thickness, the particle length decreases faster than the particle thickness, decreasing the aspect ratio.

The average particle lengths for all these nanocomposites are larger than those observed for nylon 6 nanocomposites, where exfoliation is near ideal, i.e., most of the particles are individual platelets [62,63]. The larger particles seen here are likely due to "skewing" of the platelets in the thicker clay bundles. However, the average particle lengths do approach the values seen in nylon 6 nanocomposites when HDPE-*g*-MA is used as the matrix, indicating near maximum exfoliation.

Ploehn and Liu accurately characterized a commonly used montmorillonite by depositing platelets on a mica surface from a very dilute suspension and then measuring the lateral dimensions by atomic force microscopy [64]. Since the lateral size or shape of the platelets is not uniform, the platelet area, *A*, was measured and its square-root was normalized by platelet thickness, *t*, to calculate an "aspect ratio". If each platelet were circular with diameter *D*, then

$$\sqrt{A}/t = \sqrt{\pi/4}(D/t) = 0.89(D/t) \quad (1)$$

Since *t* is approximately 1 nm, the most probable lateral dimension is in the range of 100–200 nm [64,65]. The average particle lengths found in this study fall below this range. However, the observed lengths reflect a random cut through irregular platelets and particles and only rarely will the maximum dimension be seen [66,67].

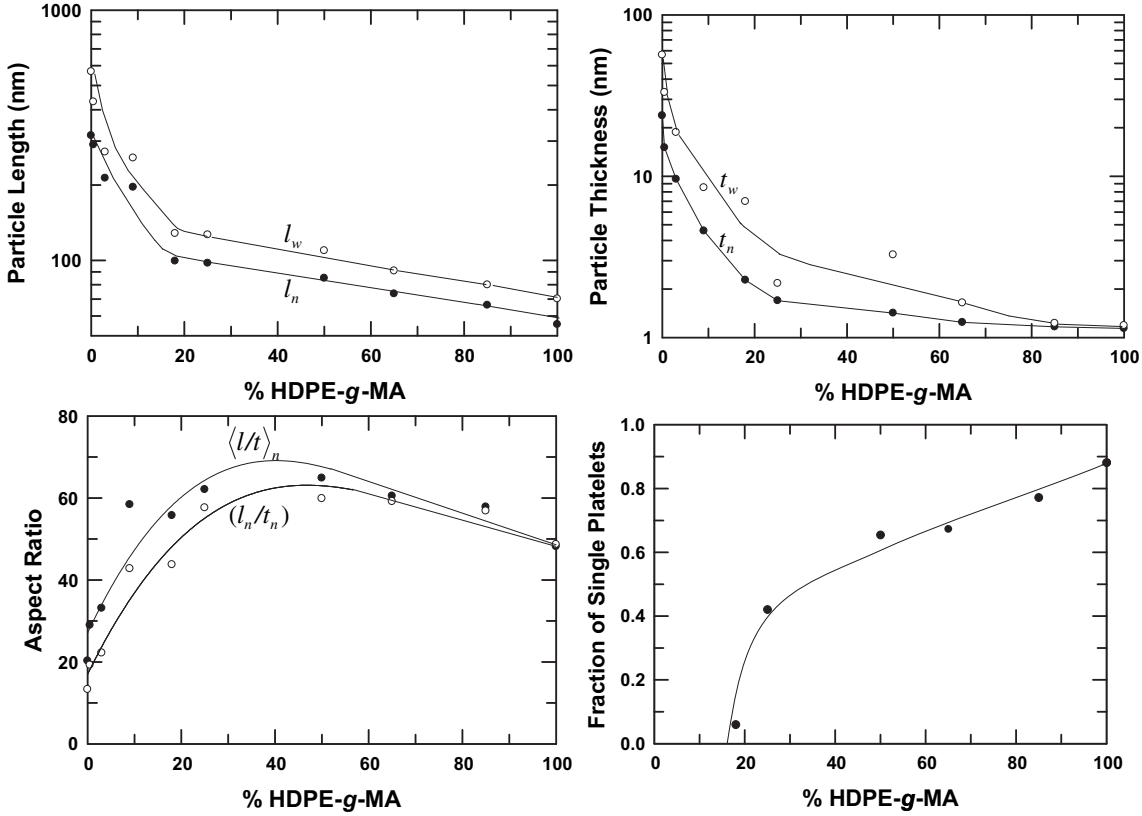

Fig. 4. The effect of HDPE-*g*-MA content on (a) particle length, (b) particle thickness, (c) number average aspect ratio and ratio of number average particle length and number average particle thickness, and (d) fraction of single platelets of HDPE/HDPE-*g*-MA/$M_2(HT)_2$ nanocomposites based on one filler population at a fixed MMT content of ~5 wt%.

3.2.3. *Wide angle X-ray scattering*

WAXS is commonly used to characterize the exfoliation structure of nanocomposites. WAXS scans of the neat organoclay ($M_2(HT)_2$) and of the skin portion of nanocomposites with ~5% MMT prepared from various polymer matrices are shown in Fig. 7. The d_{001} peak intensity decreases with increasing HDPE-*g*-MA content and disappears for nanocomposites with >50% HDPE-*g*-MA in the polymer matrix, suggesting a highly exfoliated structure. The d_{001} peak for HDPE-based nanocomposites is shifted slightly to the right of the peak for the neat organoclay. For nanocomposites with HDPE-*g*-MA compatibilizer, the peak shifts slightly to the left of the HDPE-based nanocomposite, but remains to the right of the peak for the neat organoclay. This shift to higher angle and lower *d*-spacing could indicate degradation of the surfactant, causing the clay galleries to collapse as surfactant mass is lost from within the galleries [16]. These differences are so small, however, that it is difficult to attach much physical meaning to them [15,61]. These results are in good agreement with the TEM analysis discussed above. The WAXS results give only limited information about morphology and TEM, though providing a clearer understanding of exfoliation levels, examines only a small volume and may not be representative of the nanocomposite as a whole. Therefore, bulk mechanical properties were measured to complement TEM and WAXS analyses [15,61].

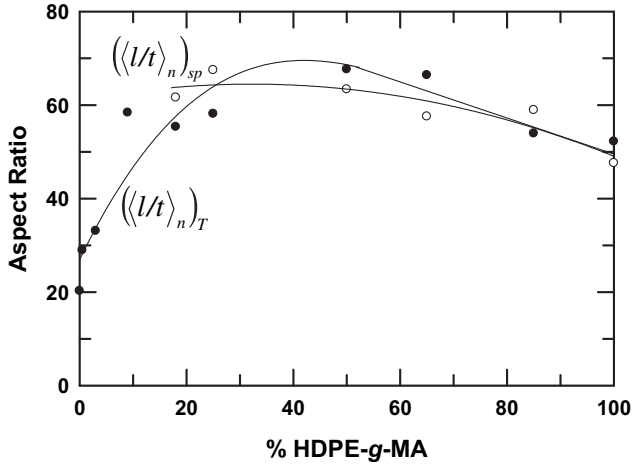

Fig. 5. The effect of HDPE-*g*-MA content on the two population number average aspect ratios accounting for tactoids and single platelets separately for HDPE/HDPE-*g*-MA/$M_2(HT)_2$ nanocomposites at a fixed MMT content of ~5 wt%.

3.3. *Mechanical properties*

Of the various mechanical properties, modulus provides the best indicator of organoclay exfoliation [1]. Modulus data are shown in Table 5 for nanocomposites with MMT contents of ~5 wt%. Fig. 8(a) shows the effect of MMT concentration on the tensile modulus of HDPE nanocomposites with various amounts of HDPE-*g*-MA. As expected, increasing MMT content results in significant improvements in modulus. Since the moduli of the neat HDPE-based polymers (E_m) vary with HDPE-*g*-MA content, examining the relative moduli (E/E_m) allows more useful comparisons. Relative modulus as a function of MMT concentration in nanocomposites with various amounts of HDPE-*g*-MA is shown in Fig. 8(b). At high MMT contents, the improvement in modulus increases rapidly with the addition of small amounts of HDPE-*g*-MA. At higher HDPE-*g*-

Table 4
Parameters used in the Mori–Tanaka two population model.[a]

HDPE-*g*-MA %	*d*-spacing (d_{001}, nm)	Vol fraction of MMT in particle (ν_{MMT})	Weight fraction of MMT in nanocomposites (%)	Number average aspect ratio for tactoids $(\langle l/t\rangle_n)_T$	Number average aspect ratio for single platelets $(\langle l/t\rangle_n)_{sp}$	Vol fraction of the tactoids in nanocomposites (ϕ_T)	Vol fraction of the single platelets in nanocomposites (ϕ_{sp})
0	2.24	0.420	5.2	20.3		0.0431	
0.5	2.21	0.425	5.2	29.0		0.0428	
3	2.24	0.420	5.2	33.1		0.0435	
9	2.27	0.414	5.2	58.4		0.0442	
18	2.30	0.409	5.2	55.3	61.6	0.0438	0.0005
25	2.33	0.404	5.2	58.1	67.5	0.0302	0.0053
50	2.33[b]	0.404	5.4	67.6	63.4	0.0201	0.0094
65	2.33[b]	0.404	5.3	66.4	57.6	0.0149	0.0115
85	2.33[b]	0.404	5.3	53.9	58.9	0.0071	0.0147
100	2.33[b]	0.404	5.4	52.2	47.6	0.0053	0.0154

[a] For 5 wt% MMT.
[b] Assumed to be equal to that of the 25% HDPE-*g*-MA nanocomposite.

MA levels, i.e., ≥5%, the increase caused by the HDPE-*g*-MA seems to be independent of the amount of HDPE-*g*-MA added.

To better understand this, the relative modulus is plotted versus the ratio of the mass of HDPE-*g*-MA to the mass of the organoclay for various MMT loadings in Fig. 9(a). The relative modulus is increased significantly for nanocomposites with an HDPE-*g*-MA/organoclay ratio of about 0.5. Increasing the ratio to 2, however, results in little further change. Kim et al. found a similar trend for PP/PP-*g*-MA/organoclay nanocomposites [15]. Further increasing the amount of HDPE-*g*-MA in the nanocomposites increases the modulus, but at a much lower rate, as shown in Fig. 9(b). Fig. 10 shows the relative moduli for nanocomposites with ~5 wt% MMT plotted against the aspect ratios, $(\overline{l_n}/\overline{t_n})$, obtained from TEM images. In general, the relative modulus increases as the aspect ratio increases. The nanocomposites with >50% HDPE-*g*-MA in the matrix, however, show a slight increase in relative modulus and a small decrease in aspect ratio. This might be explained by the decreased modulus of the matrix, allowing for higher improvements in relative modulus [35,38,56,63,68].

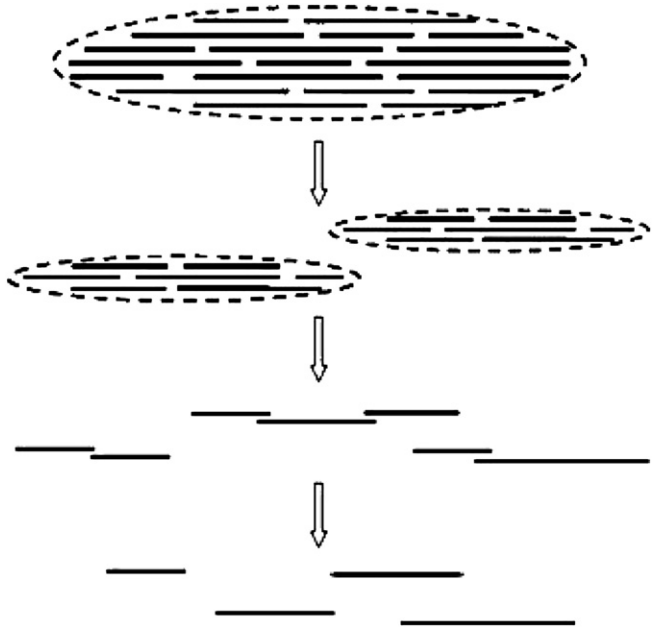

Fig. 6. Schematic illustration of the change of effective particle length and thickness with increasing HDPE-*g*-MA content.

The yield strength increases upon addition of MMT, as shown in Fig. 11(a). Also, the addition of small amounts of HDPE-*g*-MA to the polymer matrix results in relatively large increases in yield strength. With HDPE-*g*-MA levels over ~15–25%, the yield strength levels off and then declines. Thus, the decreased yield strength of the matrix offsets, in part, the benefits associated with improved organoclay exfoliation.

Elongation at break data are presented in Fig. 11(b). Nanocomposites with low MMT levels (<3 wt%) were too ductile to determine the breaking point using the available equipment. The elongation at break decreases with the addition of MMT and increasing the amount of HDPE-*g*-MA accelerates this decrease. Thus, enhanced exfoliation leads to less ductile nanocomposites.

Fracture toughness measured by the Izod impact strength is an important property for some applications. Polymer nanocomposites based on polyolefins have been reported to have different impact values for the gate end and far end of injection-molded Izod bars [27,43,69]. As with the bars of neat polymer, the fracture energy decreases for the nanocomposites from the gate end to the middle and from the middle to the far end (Fig. 12). This could be the result of differences in the molecular orientation, crystal orientation, and percent crystallinity as discussed above.

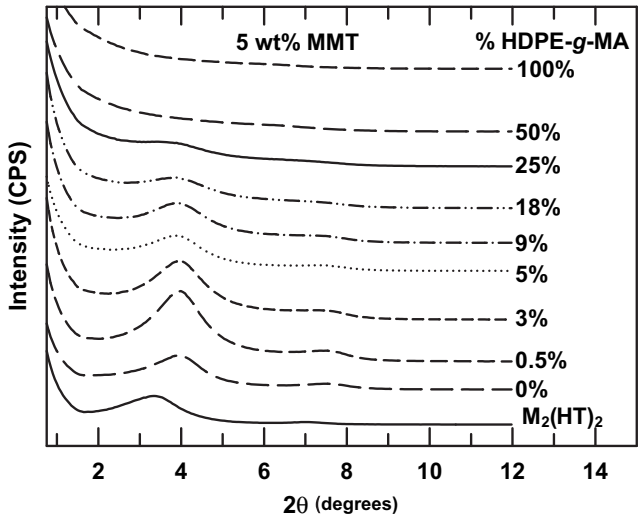

Fig. 7. WAXS scans of pristine organoclay, $M_2(HT)_2$, and nanocomposites containing ~5 wt% MMT formed from HDPE/HDPE-*g*-MA copolymers with various HDPE-*g*-MA contents. The curves are vertically offset for clarity.

Table 5
Modulus results for nanocomposites with MMT contents of ~5 wt%.

HDPE-*g*-MA %	*E* (GPa)	E_m (GPa)	E/E_m
0	1.38	1.12	1.23
0.5	1.44	1.10	1.31
3	1.64	1.17	1.40
5	1.65	1.12	1.48
9	1.68	1.17	1.44
18	1.68	1.14	1.47
25	1.78	1.15	1.54
50	1.60	1.07	1.49
65	1.52	1.00	1.54
85	1.48	0.96	1.54
100	1.51	0.98	1.55

Similarly, differences in organoclay platelet orientation may contribute. As shown in Fig. 12, impact strength generally decreases as MMT content increases regardless of the portion of the bar tested. Addition of small amounts of MMT (1.5%) results in a large decrease in impact strength relative to that of the matrix polymer. As the MMT content is increased from 1.5 wt% to 7 wt%, the impact strength decreases gradually for nanocomposites with low HDPE-*g*-MA content (<~25%). Nanocomposites with higher HDPE-*g*-MA content (Fig. 12(c) and (d)), show a slight minimum in impact strength (~3 wt%) measured at the middle and the gate end.

The Izod impact strength of nanocomposites with various clay loadings is plotted in Fig. 13(a) versus the ratio of HDPE-*g*-MA to organoclay. The maximum fracture energy occurs for an HDPE-*g*-MA/organoclay ratio between 0.5 and 1. The fracture energy recorded in an impact test reflects the integration of the resisting force of the sample over the range of the sample deflection. Raising the HDPE-*g*-MA/organoclay ratio improves the exfoliation, increasing the forces due to the high modulus and yield strength but decreasing the ductility. Although high levels of exfoliation tend to decrease the impact energy [13,50,70–72], in some cases the increase of force outweighs the decrease in ductility [16,73–75]. In this work, it appears that the initial addition of HDPE-*g*-MA improves the clay exfoliation and, hence, the modulus, to a greater extent than it decreases the ductility. Further increasing the HDPE-*g*-MA/organoclay ratio, however, lowers the impact strength below the pure HDPE level. As shown in Fig. 13(b), there is not much change at higher levels of HDPE-*g*-MA.

4. Composite model predictions of modulus

Theoretical modeling is an attractive approach for the design of polymer composite systems, and numerous models [68,76–78] have been proposed for predicting the properties of composites and for correlating experimental data with such predictions. Previous papers [35,38,43,53,62,63] have demonstrated such models can be useful for composites with nanosized fillers. However, numerous assumptions are made when using such models. For example, it is assumed that the polymer matrix is not affected by the presence of the filler, that the filler is of uniform dimensions and is perfectly aligned, that the matrix and filler are isotropic, that the matrix and

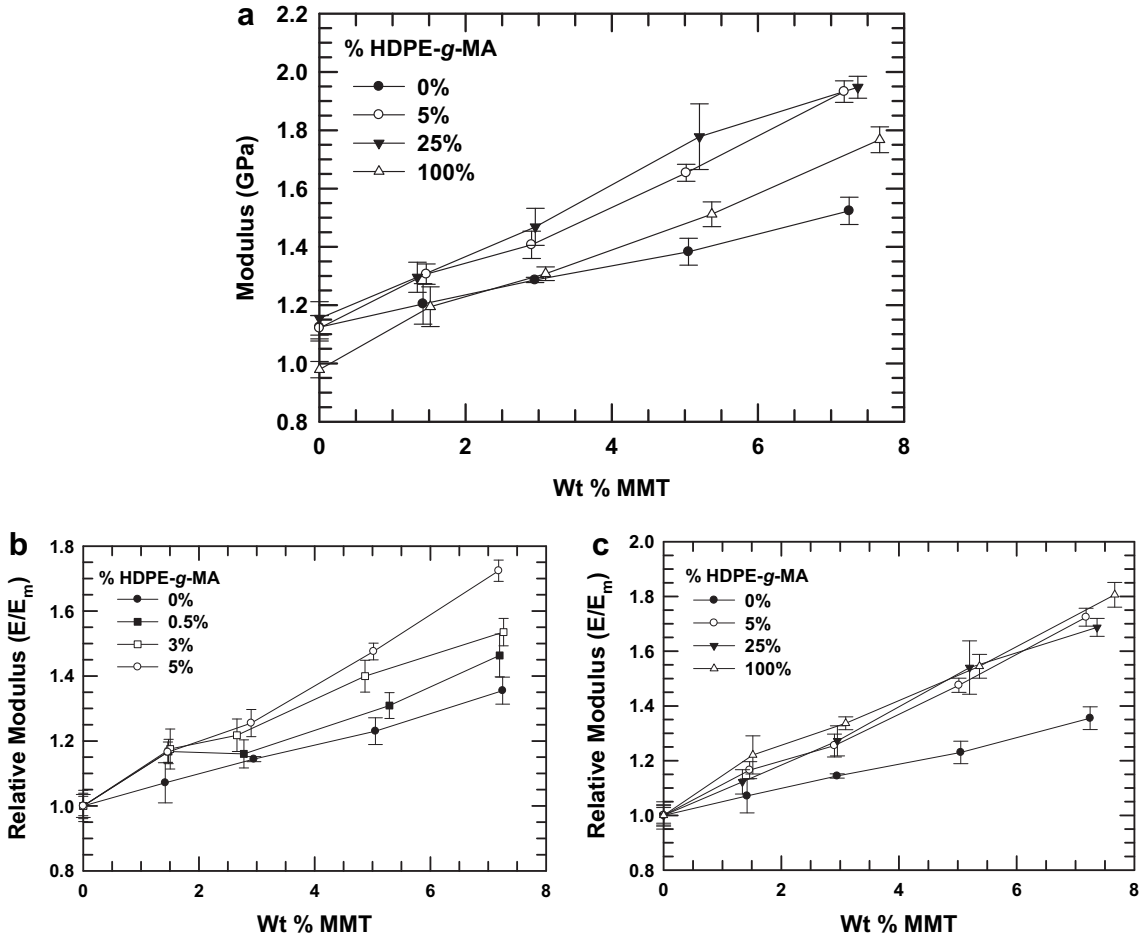

Fig. 8. Modulus (a) and relative modulus ((b) and (c)) as a function of montmorillonite content for HDPE-based nanocomposites with varying levels of HDPE-*g*-MA.

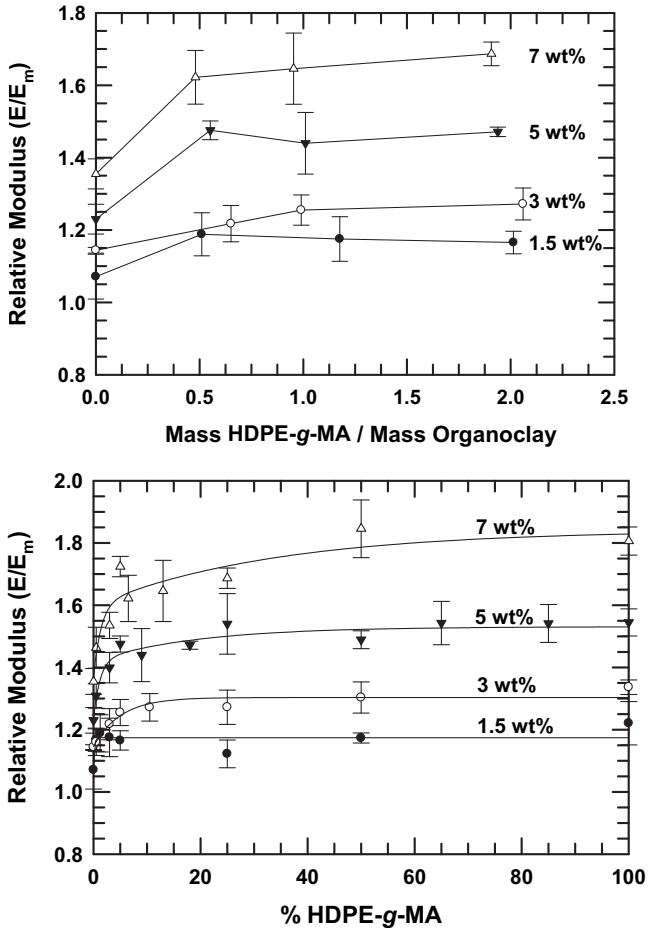

Fig. 9. Relative modulus for HDPE-based nanocomposites with various MMT loadings versus the ratio of HDPE-*g*-MA to organoclay (a) and the percent of HDPE-*g*-MA in the polymer matrix (b).

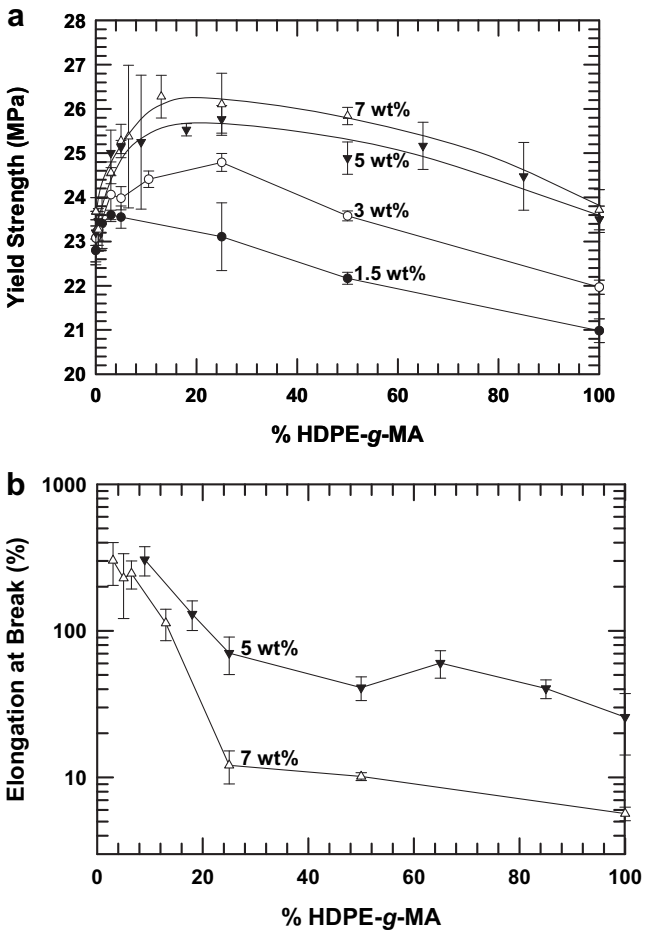

Fig. 11. Yield strength (a) and elongation at break (b) for HDPE-based nanocomposites with various MMT loadings versus the percent of HDPE-*g*-MA in the polymer matrix.

filler are well bonded, and that there are no particle–particle interactions or agglomerations [63]. Both the Halpin–Tsai equations and the Mori–Tanaka theory are used in this paper to explore the relationship between particle aspect ratio and experimental modulus.

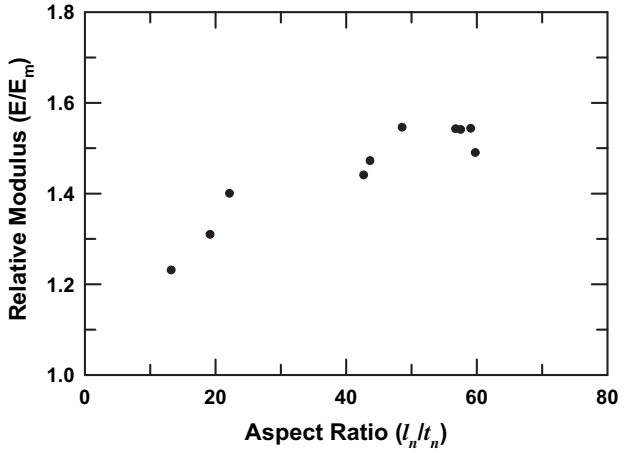

Fig. 10. Relative modulus versus the ratio of the single population number average particle length and number average particle thickness of HDPE/HDPE-*g*-MA/$M_2(HT)_2$ nanocomposites at a fixed MMT content of ~5 wt%.

The Halpin–Tsai equations can be used to predict the tensile modulus of nanocomposites from the neat component properties and the particle aspect ratios as determined by quantitative particle analysis of TEM images. The expression for the longitudinal tensile modulus [38,63,79] is

$$\frac{E^{(H-T)}}{E_m} = \frac{1 + 2(l/t)\phi_p\eta}{1 - \phi_p\eta} \tag{2}$$

where E_p and E_m are the modulus values of the filler particle and matrix polymer, respectively, ϕ_p is the volume fraction of the filler particles, (l/t) represents the filler aspect ratio, and η is given by

$$\eta = \frac{(E_p/E_m) - 1}{(E_p/E_m) + 2(l/t)} \tag{3}$$

The Mori–Tanaka average stress theory [80] is based on the principles of Eshelby's inclusion model for predicting an elastic stress field in and around an ellipsoidal particle in an infinite matrix [81]. To account for finite filler concentrations, however, Mori and Tanaka [80], considered a non-dilute composite of many identical spheroidal particles that cause the matrix to experience an average stress different from the applied stress. The volume average stress over the entire composite was forced to equal the applied stress to satisfy equilibrium conditions. Tandon and Weng [82] used this assumption together with Eshelby's solution to derive complete analytical solutions for the elastic moduli of an isotropic matrix filled with aligned spheroidal inclusions. For a composite with disk-

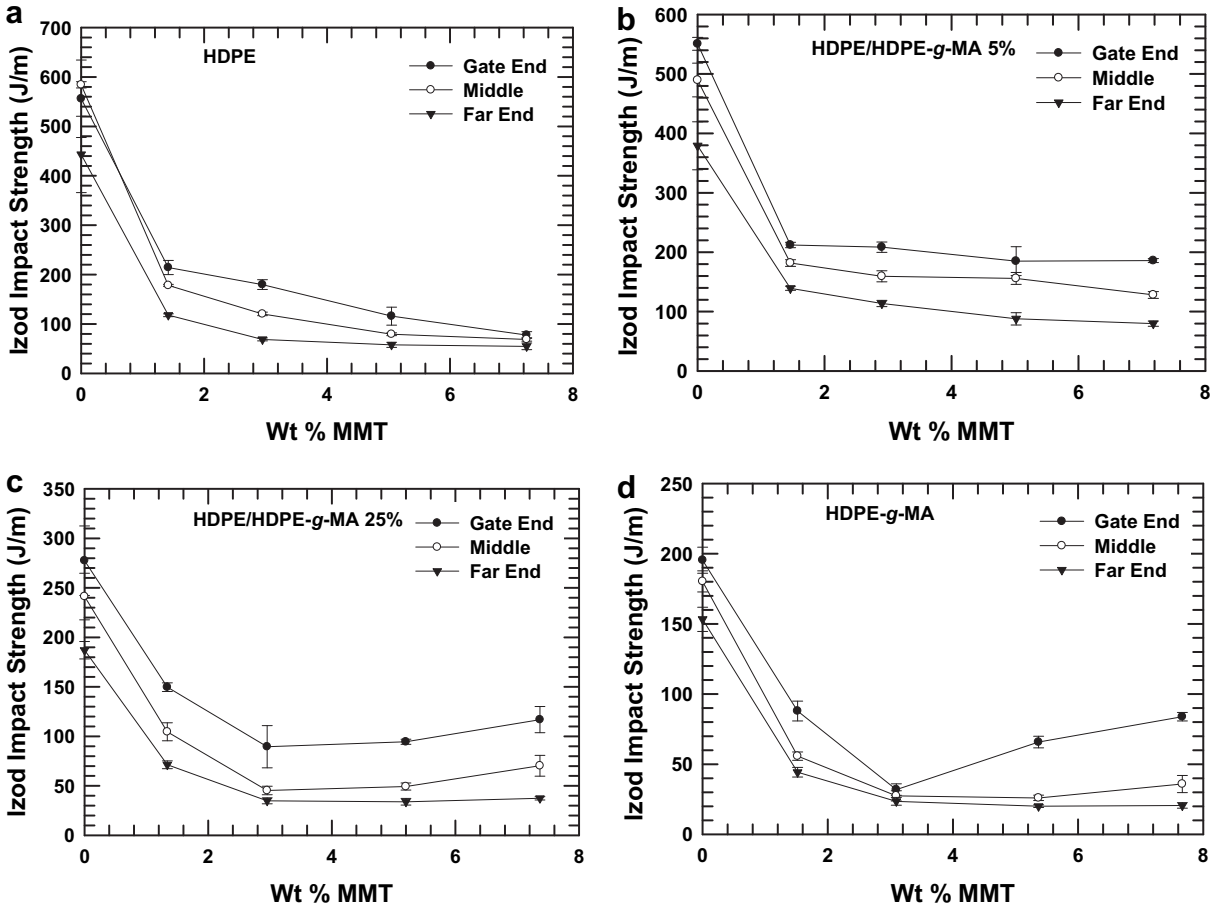

Fig. 12. Izod impact strength as tested at the gate end, middle, and far end for nanocomposites based on HDPE/HDPE-*g*-MA with 0% (a), 5% (b), and 25% (c) HDPE-*g*-MA in the polymer matrix versus MMT content.

shaped inclusions, the relative modulus parallel to either major axis of the disk-like spheroids is

$$\frac{E^{(\mathrm{M-T})}}{E_\mathrm{m}} = \frac{2A}{2A + \phi_\mathrm{p}[-2\nu_\mathrm{m}A_3 + (1-\nu_\mathrm{m})A_4 + (1+\nu_\mathrm{m})A_5 A]} \tag{4}$$

where ϕ_p is the volume fraction of filler, ν_m is Poisson's ratio of the matrix, and A, A_3, A_4, A_5, are functions of Eshelby's tensor and the properties of the filler and the matrix, specifically Young's modulus, Poisson's ratio, filler concentration, and filler aspect ratio; complete details of these equations are given elsewhere [82]. The Poisson's ratios of the matrix, ν_m, and of the organoclay, ν_p, are assumed to be 0.35 and 0.20 respectively [63,83,84].

In comparing the results of the Halpin–Tsai equations and the Mori–Tanaka theory, there are important differences between the two theories to bear in mind. The Mori–Tanaka theory treats disks as ellipsoidal particles, while the Halpin–Tsai equations treat disks as rectangular platelets. Since the length and, therefore, the aspect ratio are not constant across a particle, the Halpin–Tsai equations assume a larger particle size than the Mori–Tanaka theory. Additionally, the Halpin–Tsai equations are independent of Poisson's ratio of the filler and the matrix [63].

In the model calculations, there are generally two ways of treating the filler particles. One is to assume good exfoliation (method 1) and treat the MMT platelets themselves as the reinforcing filler particles. In this case, $E_\mathrm{p} = E_\mathrm{MMT} = 178$ GPa [63] and $\phi_\mathrm{p} = \phi_\mathrm{MMT} = 0.0175$ at 5 wt% MMT.

Another way is to consider the partially exfoliated clay particles as parallel arrangements of MMT platelets and gallery material as described in previous reports [15,35,38,63,79,85] (method 2). The tensile modulus of such an effective particle is often assumed to be given by the following rule of mixtures

$$E_\mathrm{p} = \nu_\mathrm{MMT}E_\mathrm{MMT} + \nu_\mathrm{gallery}E_\mathrm{gallery} \tag{5}$$

where ν_MMT and ν_gallery are the volume fraction of montmorillonite and of the gallery space in the effective particle, while E_MMT and E_gallery are their corresponding moduli. The volume fraction of MMT platelets in the particle, ν_MMT, is calculated as the ratio of the thickness of an individual platelet and the d-spacing of the nanocomposite as determined by the WAXS analysis

$$\nu_\mathrm{MMT} = \frac{t_\mathrm{platelet}}{d_{001}} \tag{6}$$

Considering that the modulus of the organic material in the gallery is significantly smaller than the modulus of the MMT platelets, Eq. (3) reduces to

$$E_\mathrm{p} = \nu_\mathrm{MMT}E_\mathrm{MMT} \tag{7}$$

The volume fraction of the filler particles in the composites can be estimated as

$$\phi_\mathrm{p} = \frac{\text{volume of MMT}}{\text{volume of nanocomposite}}\frac{\text{volume of filler particle}}{\text{volume of MMT}} = \frac{\phi_\mathrm{MMT}}{\nu_\mathrm{MMT}} \tag{8}$$

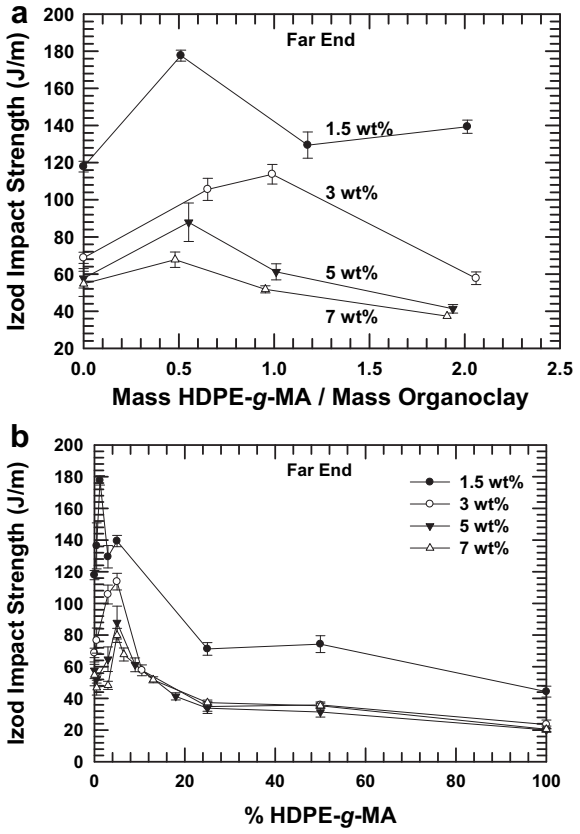

Fig. 13. Izod impact strength measured at the far end for HDPE-based nanocomposites with various MMT loadings versus the ratio of HDPE-*g*-MA to organoclay (a) and the percent of HDPE-*g*-MA in the polymer matrix (b).

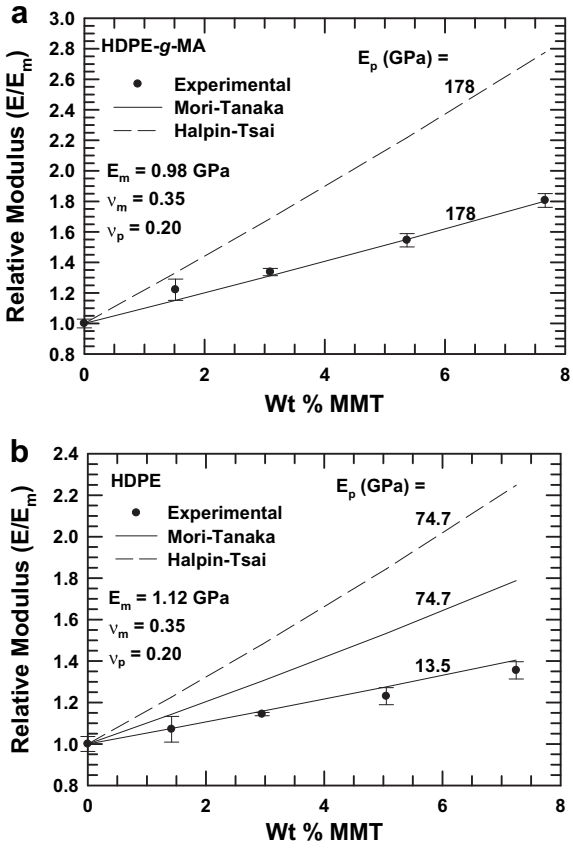

Fig. 14. Comparison of experimental relative modulus with predictions by the one population model using Halpin–Tsai equations and Mori–Tanaka theory for HDPE-*g*-MA based (a) and HDPE-based (b) nanocomposites versus MMT content.

Thus, the d_{001} values determined by WAXS are needed for predictions using method 2. It is easy to determine the *d*-spacing from WAXS scans of nanocomposites based on matrices with ≤25% HDPE-*g*-MA; however, at higher levels of HDPE-*g*-MA, no distinctive peaks are found in the WAXS scans. Thus, in order to apply the partially exfoliated particle assumption to nanocomposites with ≥50% HDPE-*g*-MA, the *d*-spacing is assumed to be equal to that of the 25% HDPE-*g*-MA nanocomposite.

The aspect ratios calculated from ~5 wt% samples are applied in the models for all clay loadings. For simplicity, the $\langle l/t\rangle_n$ aspect ratio is used in all predictions shown. Different aspect ratios give similar, though different, results.

Since TEM and subsequent image analysis reveal that nanocomposites with HDPE-*g*-MA matrices are almost completely exfoliated, method 1 can be used for the model predictions. Fig. 14(a) compares the predictions for relative modulus as a function of MMT loading obtained from both the Halpin–Tsai and Mori–Tanaka methods with experimental data. The Mori–Tanaka method describes the data well while the Halpin–Tsai method gives significantly higher results. It appears that the Mori–Tanaka method is more applicable in this system.

Method 2 is used for nanocomposites with HDPE matrices since they are not well exfoliated. Fig. 14(b) shows Halpin–Tsai and Mori–Tanaka predictions with experimental data for nanocomposites with an HDPE matrix. Both methods substantially overestimate the experimental relative modulus. One explanation could be that the particle modulus (E_p) is overestimated by Eq. 7. Because the Mori–Tanaka theory predicts both the exfoliated and the non-exfoliated cases better, it was selected to be the base method for the remaining predictions. If the value of E_p used in method 2 is arbitrarily reduced from 74.7 GPa, as estimated from Eq. (7), to 13.5 GPa, a much better fit of the experimental points is attained, as shown in Fig. 14(b). The lower apparent modulus for the tactoids suggests that Eq. (7) grossly overestimates the stress transfer between platelets in the tactoids.

Nanocomposites with ≥25% HDPE-*g*-MA consist of both organoclay tactoids and dispersed single platelets. As shown, these distinct particles have different effects on the mechanical properties of the nanocomposite and separate methods are needed to predict their properties. When both particle types exist in a single nanocomposite, they should be considered separately in a two population model to more accurately predict the experimental modulus. Thus, the aspect ratios for single platelets and the aspect ratios of the remaining tactoids are both employed in the model. The volume fractions of filler in tactoids (ϕ_T) and in single platelets (ϕ_{sp}) can be estimated by multiplying the fraction of the particle areas by the volume fraction of MMT as shown in

$$\phi_T = \phi_{MMT}\frac{\sum_i (l_i t_i)_T}{\sum_i (l_i t_i)_{sp} + \nu_{MMT}\sum_i (l_i t_i)_T} \tag{9}$$

and

$$\phi_{sp} = \phi_{MMT}\frac{\sum_i (l_i t_i)_{sp}}{\sum_i (l_i t_i)_{sp} + \nu_{MMT}\sum_i (l_i t_i)_T} \tag{10}$$

where the subscripts T and sp indicate the parameters for the tactoids and the single platelets respectively and ν_{MMT} is the

volume fraction of MMT in the effective particle, as calculated in Eq. (6). Fig. 15 shows the filler volume fractions versus the HDPE-*g*-MA content of the matrix. Clearly, the volume fraction of tactoids, ϕ_T, decreases while the volume fraction of single platelets, ϕ_{sp}, increases with increased levels of HDPE-*g*-MA, reflecting improved exfoliation.

The contributions to the relative modulus of the tactoids and the single platelets are calculated by substituting the appropriate particle parameters into Eq. (4) as shown in

$$\frac{E_T^{(M-T)}}{E_m} = \frac{2A_T}{2A_T + \phi_T\left[-2\nu_m A_{3,T} + (1-\nu_m)A_{4,T} + (1+\nu_m)A_{5,T}A_T\right]} \tag{11}$$

and

$$\frac{E_{sp}^{(M-T)}}{E_m} = \frac{2A_{sp}}{2A_{sp} + \phi_{sp}\left[-2\nu_m A_{3,sp} + (1-\nu_m)A_{4,sp} + (1+\nu_m)A_{5,sp}A_{sp}\right]} \tag{12}$$

The particle moduli used for the tactoids and single platelets are 13.5 GPa and 178 GPa respectively, as suggested above. The Poisson's ratio for both tactoids and single platelets is assumed to be 0.20. Although the Poisson's ratio of the tactoids is likely somewhat higher than that of the single platelets, the model is insensitive to Poisson's ratio of both the matrix and the filler within the range of 0.20 and 0.40. The total relative modulus of the nanocomposite is calculated by adding the tactoid and single platelet contributions and subtracting one to avoid double counting the matrix contribution as follows

$$\frac{E^{(M-T)}}{E_m} = \frac{E_T^{(M-T)}}{E_m} + \frac{E_{sp}^{(M-T)}}{E_m} - 1 \tag{13}$$

The parameters used in the two population Mori–Tanaka model for nanocomposites containing ~5 wt% MMT are listed in Table 4.

Fig. 16(a) and (b) show the resulting predictions by the two population Mori–Tanaka model and the experimental points for nanocomposites with 25% and 50% HDPE-*g*-MA respectively. The predictions fit the data well in both cases, indicating that such a two particle population model appears to be most appropriate for this system. That is, treating tactoids and single platelets separately rather than averaging them together proves to be a more accurate way to model these nanocomposite properties.

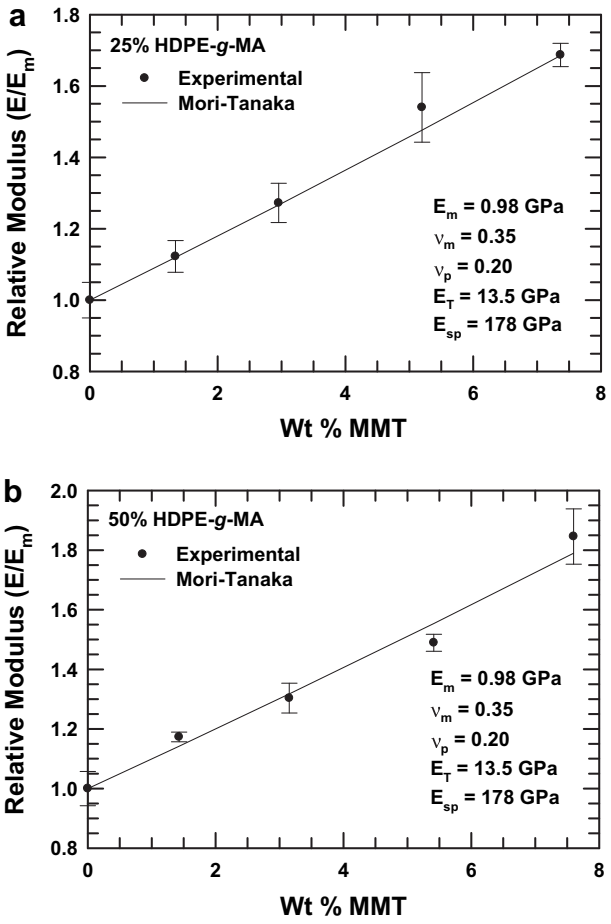

Fig. 16. Comparison of experimental relative modulus with the predictions by the two population Mori–Tanaka model accounting for tactoids and single platelets separately for HDPE-based nanocomposites with 25% (a) and 50% (b) HDPE-*g*-MA in the polymer matrix versus MMT content.

To see how well this model works over the entire range of composition of HDPE/HDPE-*g*-MA blends, the two population Mori–Tanaka predictions and experimental data for nanocomposites of 5 wt% MMT are shown in Fig. 17. The model predictions reasonably fit the experimental data over the entire range of

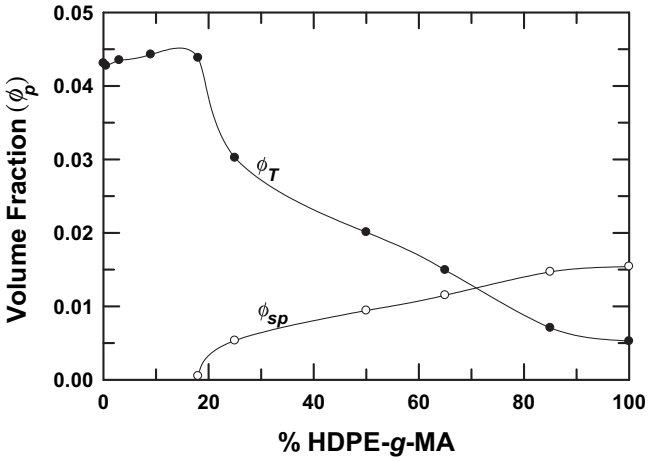

Fig. 15. Filler volume fractions for tactoids and single platelets used in the two population Mori–Tanaka model for HDPE/HDPE-*g*-MA/$M_2(HT)_2$ nanocomposites at a fixed MMT content of ~5 wt% versus the percent of HDPE-*g*-MA in the polymer matrix.

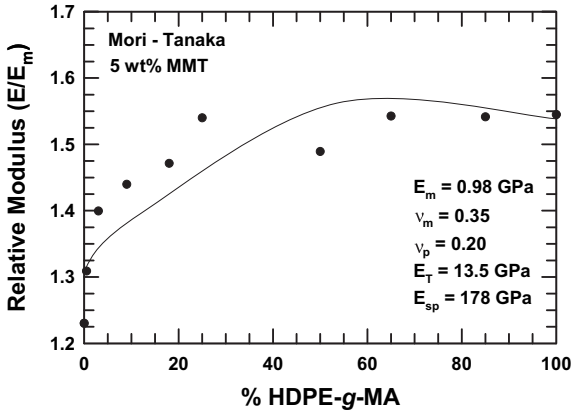

Fig. 17. Comparison of experimental relative modulus with the predictions by the two population Mori–Tanaka model accounting for tactoids and single platelets separately for HDPE/HDPE-*g*-MA/$M_2(HT)_2$ nanocomposites at a fixed MMT content of ~5 wt% versus the percent of HDPE-*g*-MA in the polymer matrix.

composition. The discrepancies are possibly due to the incomplete orientation of the clay platelets and inadequate parameter estimations for the volume fraction and modulus of the effective particles [15,43].

5. Conclusion

Nanocomposites formed from blends of HDPE and HDPE-*g*-MA and $M_2(HT)_2$ organoclay were melt processed to explore the extent of exfoliation and the mechanical properties over the entire range of matrix composition. WAXS and TEM coupled with detailed particle analysis were used to determine the effect of HDPE-*g*-MA content on exfoliation. TEM images show drastic improvements in exfoliation with initial amounts of HDPE-*g*-MA while further addition of HDPE-*g*-MA gives little visible change. Particle analysis, however, shows that the fraction of single platelets increases at a steady rate for nanocomposites with HDPE-*g*-MA contents $\geq$25%. As the HDPE-*g*-MA content increases, particle aspect ratio initially increases drastically, reaches a maximum, and slightly decreases, due to the particle thickness limit of a single platelet (0.94 nm).

Similarly, the relative modulus initially improves significantly with increased levels of HDPE-*g*-MA, while greater HDPE-*g*-MA content only gives a slight increase. The slight increase in relative modulus in spite of a slight decrease in aspect ratio might be due to the decreased modulus of the matrix, facilitating improvements in relative modulus. Modulus increases and Izod impact strength decreases as MMT levels increase, for all HDPE-*g*-MA levels. Fracture energy reaches a maximum at low HDPE-*g*-MA levels, decreases below the value for the pure HDPE nanocomposite, and levels off at higher HDPE-*g*-MA content. Initially, adding HDPE-*g*-MA to the matrix results in significantly improved exfoliation and properties. Further addition of HDPE-*g*-MA, however, lowers the matrix properties enough to offset the benefits of enhanced matrix/organoclay interactions.

Because of the different reinforcement effects of partially exfoliated organoclay tactoids and single platelets, particle analysis was also performed on these two populations separately. A composite model based on the Mori–Tanaka theory was developed to treat organoclay tactoids and single platelets as two separate types of fillers. This two population Mori–Tanaka model gives rather good quantitative agreement between the predicted values of modulus calculated from the TEM results and that measured experimentally.

Acknowledgements

The authors sincerely thank Southern Clay Products, Inc. for providing organoclay materials and Mr. Tony Gonzalez for his help with WAXS analyses. We thank LyondellBasell and the E.I. Du Pont Co. for providing the polymers that made this investigation possible.

References

[1] Fornes TD, Yoon PJ, Hunter DL, Keskkula H, Paul DR. Polymer 2002;43(22):5915–33.
[2] Giannelis EP. Applied Organometallic Chemistry 1998;12(10–11):675–80.
[3] Lee H-S, Fasulo PD, Rodgers WR, Paul DR. Polymer 2005;46(25):11673–89.
[4] Bharadwaj RK. Macromolecules 2001;34(26):9189–92.
[5] Messersmith PB, Giannelis EP. Journal of Polymer Science Part A: Polymer Chemistry 1995;33(7):1047–57.
[6] Yano K, Usuki A, Okada A, Kurauchi T, Kamigaito O. Journal of Polymer Science Part A: Polymer Chemistry 1993;31(10):2493–8.
[7] Lee H-S, Fasulo PD, Rodgers WR, Paul DR. Polymer 2006;47(10):3528–39.
[8] Kim DH, Fasulo PD, Rodgers WR, Paul DR. Polymer 2008;49(10):2492–506.
[9] Gilman JW. Applied Clay Science 1999;15(1–2):31–49.
[10] Gilman JW, Kashiwagi T, Brown JET, Lomakin S, Giannelis EP, Manias E. International SAMPE Symposium and Exhibition 1998;43:1053.
[11] Bourbigot S, Le Bras M, Dabrowski F, Gilman JW, Kashiwagi T. Fire and Materials 2000;24(4):201–8.
[12] Fornes TD, Hunter DL, Paul DR. Macromolecules 2004;37(5):1793–8.
[13] Fornes TD, Yoon PJ, Keskkula H, Paul DR. Polymer 2001;42(25):9929–40.
[14] Hotta S, Paul DR. Polymer 2004;45(22):7639–54.
[15] Kim DH, Fasulo PD, Rodgers WR, Paul DR. Polymer 2007;48(18):5308–23.
[16] Shah RK, Hunter DL, Paul DR. Polymer 2005;46(8):2646–62.
[17] Hasegawa N, Kawasumi M, Kato M, Usuki A, Okada A. Journal of Applied Polymer Science 1998;67(1):87–92.
[18] Kawasumi M, Hasegawa N, Kato M, Usuki A, Okada A. Macromolecules 1997;30:6333–8.
[19] Varela C, Rosales C, Perera R, Matos M, Poirier T, Blunda J, et al. Polymer Composites 2006;27(4):451–60.
[20] López-Quintanilla ML, Sánchez-Valdés S, Ramos de Valle LF, Guedea Miranda R. Polymer Bulletin 2006;57(3):385–93.
[21] Galgali G, Ramesh C, Lele A. Macromolecules 2001;34(4):852–8.
[22] Reichert P, Nitz H, Klinke S, Brandsch R, Thomann R, Mülhaupt R. Macromolecular Materials and Engineering 2000;275(1):8–17.
[23] Cui L, Paul DR. Polymer 2007;48(6):1632–40.
[24] Lertwimolnun W, Vergnes B. Polymer 2005;46(10):3462–71.
[25] Hasegawa N, Okamoto H, Kawasumi M, Kato M, Tsukigase A, Usuki A. Macromolecular Materials and Engineering 2000;280–281(1):76–9.
[26] Li X, Wang C-Y, Fang L, Liu L-Z. Harbin Ligong Daxue Xuebao 2003;8(2):90–3.
[27] Shah RK, Cui L, Williams KL, Bauman B, Paul DR. Journal of Applied Polymer Science 2006;102(3):2980–9.
[28] Filippi S, Marazzato C, Magagnini P, Famulari A, Arosio P, Meille SV. European Polymer Journal 2008;44(4):987–1002.
[29] Wang KH, Choi MH, Koo CM, Choi YS, Chung IJ. Polymer 2001;42(24):9819–26.
[30] Gopakumar TG, Lee JA, Kontopoulou M, Parent JS. Polymer 2002;43(20):5483–91.
[31] Liang G, Xu J, Bao S, Xu W. Journal of Applied Polymer Science 2004;91(6):3974–80.
[32] Morawiec J, Pawlak A, Slouf M, Galeski A, Piorkowska E, Krasnikowa N. European Polymer Journal 2005;41(5):1115–22.
[33] Zhang M, Sundararaj U. Macromolecular Materials and Engineering 2006;291(6):697–706.
[34] Mainil M, Alexandre M, Monteverde F, Dubois P. Journal of Nanoscience and Nanotechnology 2006;6:337–44.
[35] Cui L, Ma X, Paul DR. Polymer 2007;48(21):6325–39.
[36] Zanetti M, Camino G, Thomann R, Mülhaupt R. Polymer 2001;42(10):4501–7.
[37] Cerezo FT, Preston CML, Shanks RA. Composites Science and Technology 2007;67(1):79–91.
[38] Shah RK, Kim DH, Paul DR. Polymer 2007;48(4):1047–57.
[39] Filippi S, Marazzato C, Magagnini P, Minkova L, Tzankova N, Francesco D, et al. Macromolecular Materials and Engineering 2006;291(10):1208–25.
[40] Huang Y, Ma X, Liang G, Wang S, Zhang Q. Polymer 2008;49(8):2085–94.
[41] Shah RK, Krishnaswamy RK, Takahashi S, Paul DR. Polymer 2006;47(17):6187–201.
[42] Shah RK, Paul DR. Macromolecules 2006;39(9):3327–36.
[43] Cui L, Troeltzsch C, Yoon PJ, Paul DR. Macromolecules 2009;42(7):2599–608.
[44] Ho RM, Su AC, Wu CH, Chen SI. Polymer 1993;34(15):3264–9.
[45] Roover BD, Sclavons M, Carlier V, Devaux J, Legras R, Momtaz A. Journal of Polymer Science Part A: Polymer Chemistry 1995;33(5):829–42.
[46] Zhang R, Zhu Y, Zhang J, Jiang W, Yin J. Journal of Polymer Science Part A: Polymer Chemistry 2005;43(22):5529–34.
[47] Borse NK, Kamal MR. Polymer Engineering & Science 2009;49(4):641–50.
[48] González-Montiel A, Keskkula H, Paul DR. Journal of Polymer Science Part B: Polymer Physics 1995;33(12):1751–67.
[49] Huang JJ, Keskkula H, Paul DR. Polymer 2006;47(2):624–38.
[50] Yoon PJ, Hunter DL, Paul DR. Polymer 2003;44(18):5323–39.
[51] Fornes TD, Yoon PJ, Keskkula H, Paul DR. Polymer 2002;43(7):2121–2.
[52] Stretz HA, Paul DR. Polymer 2006;47(26):8527–35.
[53] Stretz HA, Paul DR, Li R, Keskkula H, Cassidy PE. Polymer 2005;46(8):2621–37.
[54] Wunderlich B, Czornyj G. Macromolecules 1977;10(5):906–13.
[55] Yoon PJ, Fornes TD, Paul DR. Polymer 2002;43(25):6727–41.
[56] Fornes TD, Paul DR. Macromolecules 2004;37(20):7698–709.
[57] Paul DR, Zeng QH, Yu AB, Lu GQ. Journal of Colloid and Interface Science 2005;292(2):462–8.
[58] Li B, Gong G, Xie B-H, Yang W, Yang M-B. Journal of Applied Polymer Science 2008;109(2):1161–7.
[59] Pantani R, Coccorullo I, Speranza V, Titomanlio G. Progress in Polymer Science 2005;30(12):1185–222.
[60] Pantani R, Coccorullo I, Speranza V, Titomanlio G. Polymer 2007;48(9):2778–90.
[61] Kim DH, Fasulo PD, Rodgers WR, Paul DR. Polymer 2007;48(20):5960–78.
[62] Chavarria F, Paul DR. Polymer 2004;45(25):8501–15.
[63] Fornes TD, Paul DR. Polymer 2003;44(17):4993–5013.
[64] Ploehn HJ, Liu C. Industrial & Engineering Chemistry Research 2006;45(21):7025–34.
[65] Paul DR, Robeson LM. Polymer 2008;49(15):3187–204.
[66] Oshinski AJ, Keskkula H, Paul DR. Polymer 1996;37(22):4891–907.
[67] Corté L, Leibler L. Polymer 2005;46(17):6360–8.
[68] Halpin JC, Kardos JL. Polymer Engineering & Science 1976;16(5):344–52.
[69] Cui L, Hunter DL, Yoon PJ, Paul DR. Polymer 2008;49(17):3762–9.
[70] Cho JW, Paul DR. Polymer 2001;42(3):1083–94.

[71] Fornes TD, Paul DR. Macromolecules 2004;37(20):7698–709.
[72] Stretz HA, Paul DR, Cassidy PE. Polymer 2005;46(11):3818–30.
[73] Chen L, Wong S-C, Liu T, Lu X, He C. Journal of Polymer Science: Part B: Polymer Physics 2004;42(14):2759–68.
[74] Wang K, Chen L, Wu J, Toh ML, He C, Yee AF. Macromolecules 2005;38(3):788–800.
[75] Yoo Y, Shah RK, Paul DR. Polymer 2007;48(16):4867–73.
[76] Hill R. Journal of the Mechanics and Physics of Solids 1965;13(4):213–22.
[77] Halpin J. Journal of Composite Materials 1969;3:732.
[78] Hill R. Proceedings of the Physical Society, London 1952;65A:349–54.
[79] Sheng N, Boyce MC, Parks DM, Rutledge GC, Abes JI, Cohen RE. Polymer 2004;45(2):487–506.
[80] Mori T, Tanaka K. Acta Metallurgica 1973;21(5):571–4.
[81] Eshelby JD. Proceedings of the Royal Society of London. Series A. Mathematical and Physical Sciences 1957;241(1226):376–96.
[82] Tandon GP, Weng GJ. Polymer Composites 1984;5(4):327–33.
[83] Hui CY, David S. Polymer Engineering & Science 1998;38(5):774–82.
[84] van Es M, Xiqiao F, van Turnhout J, van der Giessen E. Comparing polymer–clay nanocomposites with conventional composites using composite modeling. In: Al-Malaika S, Golovoy A, Wilkie C, editors. Specialty polymer additives: principles and applications. London: Blackwell Science; 2001 [chapter 21].
[85] Brune DA, Bicerano J. Polymer 2002;43(2):369–87.